

# BERS: Locally Optimal Continuous Algorithm for Maritime Weather Routing with Just-in-Time Arrival

Daniel Precioso<sup>a</sup>, Francisco Suárez<sup>a</sup>, Javier Jiménez de la Jara<sup>b</sup>, Rafael Ballester-Ripoll<sup>a</sup>, David Gómez-Ullate<sup>a</sup>

<sup>a</sup>*School of Science and Technology, IE University, Paseo de la Castellana, 259, 28046, Madrid, Spain*

<sup>b</sup>*Department of Computer Science, Higher School of Engineering, Universidad de Cádiz, Av. Universidad de Cádiz, 10, 11519, Puerto Real, Cádiz, Spain*

---

## Abstract

Maritime weather routing must optimize route geometry under dynamic wind-wave conditions, obstacle constraints, and fixed-arrival requirements. We present Bézier Evolve and Refine Strategy (BERS), a two-stage framework that combines global evolutionary search (CMA-ES) with local variational refinement (FMS). Routes are parametrized as Bézier curves and evaluated with dense along-path sampling, enabling smooth trajectories while preserving practical feasibility constraints and accounting for mid-segment effects. We evaluate BERS on synthetic benchmarks designed to stress seven operational criteria: continuity, obstacle avoidance, dynamic adaptation, flexible objective design, constant-load feasibility, just-in-time arrival, and local optimality. Across these tests, BERS matches or improves published baselines while maintaining robust convergence under challenging flow fields and land geometries. We then validate the method on real ocean data using hourly ERA5 forcing over 366 daily departures in 2024 for two trans-oceanic corridors (Atlantic and Pacific), with a physics-based model of an 88 m cargo vessel with optional rigid wingsails. In real-ocean experiments, route optimization alone reduces mean propulsive energy by 23–59% versus great-circle baselines of the same propulsion mode. Combined with wind-assisted propulsion, total savings reach up to 75%. These results show that BERS provides a practical and scalable foundation for just-in-time, energy-efficient weather routing in maritime decarbonization workflows.

*Keywords:* Maritime decarbonization, Wind-assisted propulsion, Evolutionary optimization, Variational refinement, Arrival-time constrained routing

---

## 1. Introduction

Weather routing is a challenging optimization problem that focuses on determining efficient maritime routes while taking into account environmental factors such as wind, waves, currents, and other dynamic meteorological conditions. Unlike traditional shortest-path problems, which operate on static networks, weather routing is complicated by continuous changes in input data and the need to balance multiple objectives [1]. This problem is of significant practical importance in modern shipping, where optimising routes can reduce fuel consumption, travel time, and emissions, while ensuring navigational

safety. A key aspect of this problem is to find solutions that balance competing goals, such as minimising travel time and fuel consumption, often within large and uncertain search spaces [2]. Advances in algorithm design and computational methods have made significant progress in the field, with meta-heuristics [3], techniques to incorporate user preferences [4, 5], and evolutionary approaches [6, 7].

Weather routing has become a key operational measure for improving both the economic and environmental performance of maritime transport. By continuously optimising the course and speed of the vessel based on forecasts of wind, waves, and currents, routing systems can reduce fuel consumption and emissions without requiring hardware modifications. According to the International Maritime Organisation (IMO) [8], the expected efficiency improvement from weather routing typically ranges between 0 and 5%, depending on the type of vessel and the characteristics of the route. More recent

---

\*Corresponding author

*Email addresses:* daniel.precioso@ie.edu (Daniel Precioso), francisco.suarez@ie.edu (Francisco Suárez), javier.jimenezdelajara@uca.es (Javier Jiménez de la Jara), rballester@faculty.ie.edu (Rafael Ballester-Ripoll), dgomezullate@faculty.ie.edu (David Gómez-Ullate)

studies report average savings of 4–7% when routing is coupled with voyage speed and ETA optimization [9, 10, 11]. Weather routing companies report average fuel savings of 5.5%, which is roughly \$ 17,700 per voyage for deep-sea bulk carriers [11]. These figures reflect the typical gain from adjusting speed and heading along an otherwise fixed route for conventional large cargo vessels; methods that optimise the full route geometry over long trans-oceanic corridors, or vessels equipped with wind-assisted propulsion systems, can achieve substantially higher savings, since the choice of route directly determines the sail utilization on top of the conventional fuel-minimization benefit.

These reductions in fuel translate directly into lower greenhouse-gas emissions: each tonne of avoided marine fuel prevents approximately 3.114 tonnes of CO<sub>2</sub> from being emitted [12, 13]. Therefore, a 5% fuel reduction on a typical 20-day ocean voyage consuming 600 t of fuel would avoid about 94 t of CO<sub>2</sub>. Given that the cost of weather-routing services and data subscriptions is modest relative to bunker expenditure, payback times are generally within a few voyages. The combination of economic incentives and regulatory pressure under initiatives such as the IMO GHG strategy reinforces the relevance of accurate and adaptive routing algorithms as a decarbonization lever in maritime operations.

Taken together, these demonstrated operational gains and decarbonization pressures underscore a central methodological gap: current routing tools are valuable, but their practical impact depends on simultaneously meeting several technical requirements. To frame this gap, we identify several key criteria that a comprehensive weather routing algorithm should ideally fulfil:

- C1 **Continuous in Space:** The algorithm must resolve environmental and constraint effects along each route segment with sufficient spatial resolution, so relevant mid-segment phenomena are not skipped. This concerns not only how trajectories are represented (grid-based or not), but also how densely conditions are evaluated between waypoints.
- C2 **Obstacle Avoidance:** Safe navigation must be ensured by avoiding landmasses, restricted zones, and other hazards.
- C3 **Dynamic Conditions:** The algorithm should adapt to changing environmental factors, such as evolving wind patterns, ocean currents, and waves.
- C4 **Flexible Cost Functions:** It should accommodate various optimization goals, such as minimising travel time, fuel consumption, safety, or a combination of them.
- C5 **Constant Engine Load:** The method must handle constant engine power operations, which reflect real ship performance and typically focus on minimizing travel time.
- C6 **Just-in-Time Arrival:** The algorithm should allow adherence to predetermined travel durations, allowing adjustments to optimize fuel savings while ensuring timely arrival.
- C7 **Local Optimality:** The approach should find the best possible solution within its neighbourhood.

Existing algorithms tend to specialize in meeting some of these criteria but often struggle to address others, resulting in trade-offs that limit their applicability. We identify three families of methods used in weather routing: variational optimization, graph-based methods, and evolutionary algorithms.

The first family of methods, **variational algorithms**, is particularly effective in modeling the continuous nature of weather and maritime geography. For instance, the discrete Newton-Jacobi (DNJ) algorithm introduced by Ferraro *et al.* [14] demonstrated strong performance in synthetic vector fields, minimising travel time under constant speed or reducing fuel consumption while meeting prescribed arrival times. This novel method was later renamed the Ferraro-Martín de Diego-Sato (FMS) algorithm and successfully applied to real-world optimization scenarios [4]. Variational methods are well-suited for finding locally optimal solutions in problems with smooth, continuous inputs. However, they are less effective in scenarios that require the imposition of additional constraints, such as obstacle avoidance. Moreover, incorporating complex cost functions can be challenging, particularly when derivatives are difficult or impossible to compute.

**Graph-based methods**, such as VISIR-2 [5], PRM [15], and SIMROUTE [16], take a different approach by discretizing the search space into a graph structure. These methods naturally excel in obstacle avoidance, as hazards can be directly accounted for during graph construction. A well-designed heuristic can also ensure that these algorithms find the best solution within the graph’s confines. However, the discretized nature of these methods limits their ability to capture the full complexity of continuous environments. Hybrid approaches, such as HADAD [4], have addressed this limitation by incorporating variational algorithms [14]. Even so, graph-based methods often struggle with enforcing global constraints, such as just-in-time arrivals, because of the incremental way in which graphs are constructed.

Reference	Algorithm	Continuous in Space	Obstacle Avoidance	Dynamic Conditions	Any Cost Function	Constant Engine Load	Just-in-Time Arrival	Local Minimum
FMS (DNJ) [14]	Variational	✓				✓	✓	✓
VISIR-2 [5]	Graph Search		✓	✓	✓			✓
PRM [15]	Graph Search		✓	✓	✓	✓		✓
SIMROUTE [16]	Graph Search		✓	✓	✓	✓		✓
HADAD [4]	Graph + Var.	✓	✓	✓	✓	✓		✓
w-MOEA/D [2]	Evolutionary	✓	✓	✓	✓	✓		
WRM [3]	Evolutionary	✓	✓	✓	✓		✓	
HNDS-MPSO [7]	Evolutionary		✓	✓	✓	✓		
Hybrid Search [6]	Evol. + Var.	✓	✓			✓		✓
BERS	Evol. + Var.	✓	✓	✓	✓	✓	✓	✓

Table 1: Representative weather-routing algorithms grouped by methodological family. A checkmark indicates that the corresponding study satisfies the stated criterion.

**Evolutionary algorithms** offer another alternative. These methods, exemplified by w-MOEA/D [2], WRM [3], and HNDS-MPSO [7], operate by generating a population of candidate solutions and iteratively refining them to favour lower-cost routes. Their strength lies in their adaptability: they can handle dynamic conditions, flexible cost functions, and additional constraints like obstacle avoidance or engine load through penalization strategies. However, because these methods rely on stochastic search processes, they cannot guarantee that the solution found will be locally optimal. The Hybrid Search strategy proposed by [6] attempts to bridge this gap by using an evolutionary algorithm for broad exploration, followed by refinement with the FMS algorithm [14] to ensure local optimality. Despite their flexibility, evolutionary methods often face challenges in handling complex obstacle configurations or strictly adhering to arrival constraints, which may cause them to fail to converge on valid solutions [6].

Although these algorithmic families have significantly advanced weather routing, no single method currently satisfies all the criteria described above. Table 1 summarizes a representative set of algorithms from each family together with the properties most relevant to our discussion. The table is not intended as an exhaustive survey; rather, it is designed to highlight the methodological gap that remains in the literature. Addressing this gap is es-

sential for developing robust weather-routing solutions that meet the operational demands of modern maritime logistics, including efficiency, safety, and environmental sustainability.

This paper introduces BERS, a hybrid weather routing algorithm that demonstrates strong performance across all seven criteria in synthetic benchmarks. Building on the exploratory flexibility of evolutionary methods and their capacity to handle various cost functions and constraints, BERS overcomes their limitations by incorporating a variational refinement step, as proposed in previous work [6]. Specifically, BERS combines the strengths of the Covariance Matrix Adaptation Evolution Strategy (CMA-ES) with the FMS method. CMA-ES is used to generate control points that define Bézier curves, representing candidate routes for the weather routing problem. To the best of our knowledge, this study is among the first to use Bézier-curve parametrization for weather routing. These candidates are then refined using the FMS method, which ensures convergence to a local minimum. This hybrid approach enables BERS to produce valid solutions under a wide range of constraints while seamlessly supporting objectives such as constant engine load or Just-in-Time arrival, tailored to the problem’s specific criteria.

BERS has been implemented in Python 3.12 and tested on a variety of vector fields from the literature, as

well as validated on real-world data. The code is publicly available on GitHub<sup>1</sup>. While full operational deployment of BERS remains future work, this paper provides an initial demonstration that a single method can address all seven criteria. A representative result is shown in Figure 1.

The remainder of this paper is organized as follows. Section 2 presents the details of our proposed optimization approach: Bézier curve parametrization, CMA-ES evolution, refinement with FMS and obstacle avoidance. Section 3 introduces the benchmark optimization problems. The results of BERS in these benchmarks are given in Section 4. Section 5 presents real-ocean experiments on two trans-oceanic corridors with a wind-assisted cargo vessel, demonstrating energy savings of up to 75% from combined route optimization and wing-sail technology. Finally, Section 6 concludes with a discussion of the results and their broader implications for future research and practical applications. Technical implementation details that are not required for the main narrative are collected in Appendix A–Appendix B.

## 2. BERS Algorithm

We propose a novel hybrid optimization framework that combines a black-box evolutionary optimizer with a continuous trajectory representation for vessel navigation. Unlike traditional stepwise pathfinding approaches, our method employs global route generation followed by iterative refinement. Specifically:

1. We choose a low-dimensional parametrization of our solution space (vessel trajectories), namely by the set of 2D  $K$ -degree Bézier curves. We apply the Covariance Matrix Adaptation Evolution Strategy (CMA-ES) [17] to explore that space and get a candidate that is hopefully close to the globally optimal trajectory.
2. We refine the best CMA-ES candidate by re-parametrizing it as a polyline with  $L$  waypoints (where  $L \gg K$ ) and applying the Ferraro-Martín de Diego-Sato (FMS) variational method [14]. This ensures smooth, feasible, and efficient routes.

The pipeline BERS is structured to target seven key criteria proposed for a comprehensive weather routing framework, with validation shown in benchmark tests, as outlined in Section 1. In the following sections, we

<sup>1</sup><https://github.com/Weather-Routing-Research/routetools>

describe each component of the algorithm and explain how it satisfies these criteria. For reference, we denote each criterion as “C#”, such as C1 for the first.

### 2.1. Parametrization with Bézier Curves

The Two-dimensional Bézier degree curves  $K$  are defined by a set of control points  $\mathbf{c}_0, \dots, \mathbf{c}_K \in \mathbb{R}^2$  [18], where the endpoints  $\mathbf{c}_0$  and  $\mathbf{c}_K$  correspond to the source and destination, and the intermediate control points  $\mathbf{c}_1, \dots, \mathbf{c}_{K-1}$  remain free for optimization. The general formula for a Bézier curve is given by [19] by

$$B(r) = (x(r), y(r)) = \sum_{k=0}^K \binom{K}{k} (1-r)^{K-k} r^k \mathbf{c}_k, \quad 0 \leq r \leq 1, \quad (1)$$

where the parameter  $r$  governs the progression along the curve, with  $r = 0$  corresponding to the source and  $r = 1$  to the destination. In weather routing applications,  $r$  can be re-parametrised as travel time  $t$ , allowing a complete spatio-temporal description of the route; this will be particularly relevant in defining the cost function in Section 2.3. A key advantage of this representation is that it allows one to generate a trajectory with arbitrarily fine resolution by adjusting the number of waypoints along the curve. This continuous formulation removes the dependency on fixed-step routing and enables dense intra-segment sampling, which is essential to avoid missing currents, hazards, or penalty contributions between waypoints. As a result, this approach directly supports C1.

Despite its conceptual simplicity, the direct polynomial form of a Bézier curve poses numerical challenges for higher-degree curves, as the computation involves powers, binomial coefficients, and floating-point arithmetic that can accumulate rounding errors. To mitigate such instabilities, we adopt the De Casteljau’s algorithm [20, 21], which incrementally constructs the curve via linear interpolations of control points:

$$\mathbf{c}_k^{(i)} := \begin{cases} \mathbf{c}_k^{(i-1)} (1-r) + \mathbf{c}_{k+1}^{(i-1)} r, & i > 0, \\ \mathbf{c}_k, & i = 0, \end{cases} \quad (2)$$

and  $B(r) = \mathbf{c}_0^{(n)}$ . This formulation decomposes the computation into simpler operations at each iteration and ensures a stable, continuously differentiable trajectory that is essential to achieve smooth, optimized routes in the BERS framework.

We implemented Bézier parametrization in Python using JAX [22] for vectorized operations and just-in-time compilation, allowing us to reshape batched control points and process multiple trajectories concurrently

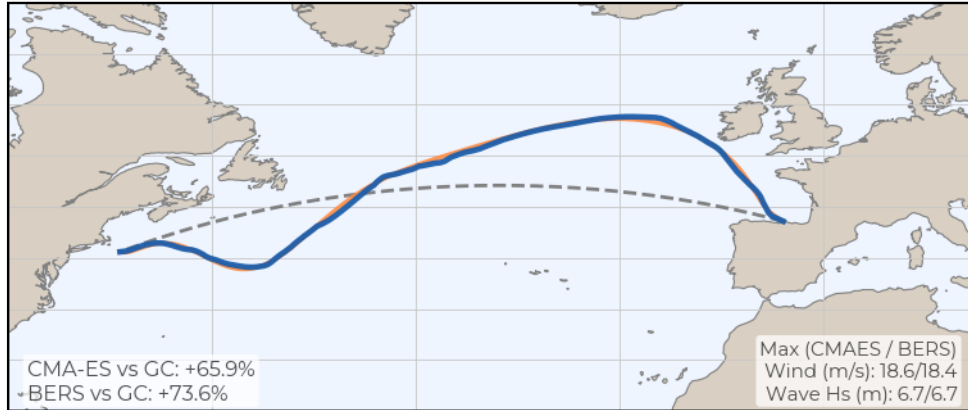


Figure 1: Representative Trans-Atlantic spring route comparing great-circle (GC), CMA-ES, and the final BERS route (CMA-ES + FMS). The refinement from CMA-ES to BERS is visually modest but operationally relevant, increasing the fuel savings from 66% to 74%. Both CMA-ES and BERS stay below the weather thresholds of wind speed (20 m/s) and wave height (7 m).

with minimal overhead. In this setup, users of BERS can specify the following parameters to balance complexity, expressiveness, and computational effort.

- **The number of control points ( $K$ );** Increasing  $K$  leads to more expressive trajectories, but slows the evolutionary algorithm and increases the risk of local optima.
- **Number of pieces ( $C$ ).** Splitting a route into more pieces provides finer local control and mitigates the need for high-degree polynomials.
- **Number of waypoints ( $L$ );** We sample the curve using  $L$  points evenly spaced in the interval  $[0, 1]$ . Higher values of  $L$  define more precise trajectories at the cost of additional computation cost.

## 2.2. CMA Evolutionary Strategy

The Covariance Matrix Adaptation Evolution Strategy (CMA-ES) is a state-of-the-art derivative-free optimization algorithm designed for continuous optimization problems [23]. CMA-ES models the search distribution as a multivariate Gaussian, iteratively updating its mean and covariance matrix to guide the search process [24].

In our BERS algorithm, the initial mean solution  $\mu_0$  corresponds to a simple straight-line trajectory connecting the source and destination. At each iteration  $\tau$ , the algorithm generates  $P$  candidate trajectories  $\{\mathbf{x}_1, \dots, \mathbf{x}_P\}$  by sampling from the current Gaussian distribution  $\mathcal{N}(\mu_\tau, \Sigma_\tau)$ .

Each candidate is then evaluated using the cost function defined in Section 2.3, which considers factors such as travel time or fuel consumption. Infeasible trajectories

such as those crossing land are penalized using the rules described in Section 2.4. Based on these evaluations, the parameters are updated to form  $\mathcal{N}(\mu_{\tau+1}, \Sigma_{\tau+1})$ , a distribution that favours the best-performing points in a way that balances exploration and exploitation of the solution space.

A key advantage of CMA-ES is its ability to escape local optima through stochastic sampling and iterative refinement [25]. Its adaptive covariance matrix guides the search towards promising regions while maintaining diversity among solutions. Additionally, the batch evaluation structure of CMA-ES is particularly beneficial for the BERS algorithm, as it enables parallel computation of hundreds of candidate trajectories simultaneously, significantly accelerating the optimization process.

For our implementation, we used the `pycma` library in Python [26], and its function `CMAEvolutionStrategy`. The following parameters can be defined to control the evolution of this algorithm:

- **Population size ( $P$ ).** The number of trajectories generated and tested at each evolutionary step. Parallelization enables simultaneous simulation of many trajectories so that the computation time grows sub-linearly with  $P$ .
- **Initial standard deviation ( $\sigma_0$ ).** This parameter controls the spread of the initial Gaussian distribution from which control points are sampled. A higher  $\sigma_0$  increases exploration by generating more diverse trajectories at the start but may slow down convergence.
- **Tolerance.** After each iteration, CMA-ES evaluates the reduction in the cost function. If this reduction

is below the specified tolerance, the evolutionary process terminates, returning the best candidate trajectory (i.e., the one with the lowest cost).

### 2.3. Cost Function

The optimizer is objective-agnostic: CMA-ES and FMS only require route-cost evaluations and do not assume a closed-form expression. For a discretized trajectory  $\Gamma = \{\mathbf{x}_n\}_{n=1}^L$ , we write the optimization target as

$$C(\Gamma) = \sum_{n=1}^{L-1} g(\mathbf{x}_n, \mathbf{x}_{n+1}; t_n), \quad (3)$$

where  $g$  can represent travel-time, energy, or any black-box operational metric. This modularity directly supports criterion C4 and is essential for the real-vessel experiments in Section 5, where proprietary performance models are used. Canonical formulations (time minimization under constant engine load, fixed-time fuel objective, and feasibility conditions) are provided in Appendix A.

### 2.4. Land Avoidance

Obstacle avoidance is a critical requirement in maritime routing. Land avoidance is treated as a hard constraint in BERS: during the CMA-ES stage, a large penalty coefficient ( $\lambda_{\text{land}} \gg 1$ ) renders any land-crossing trajectory uncompetitive; during the FMS stage, any proposed waypoint displacement that would place a segment on land is unconditionally rejected (Section 2.5). Specifically, the land contribution to the cost function is a penalization term proportional to the cumulative land-traversed distance. Let  $\Gamma = \{\mathbf{x}_n\}_{n=1}^L$  denote a candidate trajectory composed of  $L$  discrete waypoints, derived from a Bézier parametrization. The penalized cost function takes the form:

$$\mathcal{J}(\Gamma) = C(\Gamma) + \lambda \cdot \mathcal{P}(\Gamma), \quad (4)$$

where  $C(\Gamma)$  is the primary objective (e.g., travel time or fuel consumption),  $\lambda \gg 1$  is a fixed penalty coefficient (set to 100 in our experiments), and  $\mathcal{P}(\Gamma)$  denotes the land-penalization functional.

To define  $\mathcal{P}(\Gamma)$ , we discretize the Bézier curve into a denser sequence of waypoints  $\{\mathbf{x}'_n\}_{n=1}^{L'}$  with  $L' > L$ , ensuring finer detection of land intersections. The environment is modelled as a binary land-water field  $M : \Omega \subset \mathbb{R}^2 \rightarrow \{0, 1\}$ , constructed via Perlin noise. The land index function is given by:

$$M(x, y) = \begin{cases} 1, & \text{if } \phi(x, y) > \tau, \\ 0, & \text{otherwise,} \end{cases}$$

where  $\phi(x, y)$  is a normalized noise scalar field and  $\tau \in (0, 1)$  is a water-level threshold, typically  $\tau = 0.7$ .

To evaluate  $M$  on the continuous domain, we employ bilinear interpolation over a regular grid, enabling  $M$  to be queried efficiently at arbitrary locations. Each candidate curve  $\Gamma$  is interpolated across segments using  $n$  subdivisions per segment. Let  $\mathbf{x}_{ij}$  denote the  $j$ -th interpolated point of segment  $i$ , and define the land indicator function:

$$\chi(\mathbf{x}_{ij}) = \begin{cases} 1, & \text{if } M(\mathbf{x}_{ij}) = 1, \\ 0, & \text{otherwise.} \end{cases}$$

The penalization term is then defined as the weighted sum of land interactions along the curve:

$$\mathcal{P}(\Gamma) = \sum_{i=1}^{L-1} \max_{j=1, \dots, n} \chi(\mathbf{x}_{ij}), \quad (5)$$

i.e., we penalize each segment that intersects land at any of its sub-points. This structure ensures that only distinct land crossings are penalized, avoiding over-penalization from continuous land traversal.

Since CMA-ES is derivative-free, we do not require differentiability of the land penalty; the segment-wise max makes  $\mathcal{P}(\Gamma)$  discontinuous at land boundaries. Although non-smooth terrain boundaries can introduce local minima, the optimizer mitigates this effect through the mutation step size  $\sigma_0$ , which controls early-stage exploration. A suitably tuned  $\sigma_0$  allows the population to explore diverse topologies and escape poor basins of attraction near complex coastlines.

Moreover, this design avoids the binary feasibility classification used in grid-based planners, instead leveraging high-resolution continuous evaluation along each segment. By sampling intermediate points ( $n$  subdivisions per segment), the method captures obstacle interactions that would otherwise be skipped between waypoints, directly supporting C1. This enables smoother, more realistic trajectories that adapt to terrain geometry while maintaining mathematical tractability and optimization efficiency.

#### 2.4.1. Additional Constraints via Penalization

Another practical advantage of BERS is that additional operational limitations can be incorporated with minimal changes. In the real-data experiments (Section 5), we use a vessel-specific extension of the objective and incorporate wind-speed and wave-height thresholds as *soft* constraints. Routes that enter conditions with significant wave height above 7 m or wind speed above 20 m/s are penalised rather than rejected outright; this

is intentional and reflects a design requirement from the vessel operator: the optimizer should strongly discourage unsafe exposure while retaining the flexibility to accept marginally adverse segments when the overall voyage benefit justifies it. An exponential penalization term is used so that values close to the threshold remain mildly admissible while the penalty grows rapidly beyond it, yielding smooth optimization behaviour near the admissible boundary.

Concretely, if  $H_n$  and  $U_n$  denote significant wave height and wind speed at segment  $n$ , we define

$$\mathcal{P}_{\text{env}}(\Gamma) = \sum_{n=1}^{L-1} [\exp(\alpha_H [H_n - 7]_+) + \exp(\alpha_U [U_n - 20]_+) - 2], \quad (6)$$

where  $[z]_+ = \max(z, 0)$  and  $\alpha_H, \alpha_U > 0$  control the steepness of the penalty growth.

The full objective then becomes

$$\mathcal{J}(\Gamma) = C(\Gamma) + \lambda_{\text{land}} \mathcal{P}_{\text{land}}(\Gamma) + \lambda_{\text{env}} \mathcal{P}_{\text{env}}(\Gamma), \quad (7)$$

with  $\mathcal{P}_{\text{land}}$  as in Equation (5).

The weather-constraint penalty is applied consistently in both optimization stages, CMA-ES and FMS. Land avoidance follows stricter logic: while CMA-ES uses the high-coefficient penalty above, FMS enforces it as a hard constraint by unconditionally rejecting land-crossing moves. This design makes the framework modular: new soft constraints can be added as penalty terms without changing the structure of the solver.

### 2.5. Trajectory Refinement with FMS

Although CMA-ES yields a path that is close to optimal within the low-dimensional Bézier parameter space (see Section 2.2), that curve can still be improved once it is examined in the full, high-resolution setting. To perform this fine-scale adjustment we employ the Ferraro-Martín de Diego-Sato (FMS) variational optimizer [14]. FMS perturbs the interior way-points so as to lower the objective while keeping the route admissible, thereby satisfying criterion C7 and ensuring that the final solution is locally as well as globally satisfactory.

Convergence of FMS toward a stationary point of the discrete Euler-Lagrange system is secured whenever the discrete Lagrangian possesses a positive-definite Hessian (cf. Thms. 10 and 14 in [27]). For the functionals considered here, we observed stable convergence under the parameter ranges used in our experiments; we therefore use FMS as a local refinement step without claiming global convexity of the discrete Lagrangian in all settings.

Denote the Bézier curve delivered by CMA-ES, once discretised, by the ordered list of vertices

$$\Gamma^{(0)} = \{(x_1, y_1), (x_2, y_2), \dots, (x_L, y_L)\}, \quad (8)$$

where indices 1 and  $L$  correspond, respectively, to the departure and arrival ports. We write  $\mathbf{x}_n = (x_n, y_n) \in \mathbb{R}^2$  for the  $n$ -th vertex and regard the subsequence  $\{\mathbf{x}_2, \dots, \mathbf{x}_{L-1}\}$  as free variables that FMS may reposition. Because the preliminary curve already avoids land (cf. Section 2.4), the task of FMS is restricted to relocating these interior vertices so as to further decrease the segment-wise objective while preserving the feasibility of every link  $\mathbf{x}_{n-1} \rightarrow \mathbf{x}_n$ .

For the discrete polyline  $\Gamma = \{\mathbf{x}_1, \dots, \mathbf{x}_L\}$  and the edge-wise objective  $g(\mathbf{x}_n, \mathbf{x}_{n+1})$  introduced in Section 2.3, FMS treats each interior vertex  $\mathbf{x}_n$  as a variable to be relocated to a new position  $\widehat{\mathbf{x}}_n$ . Stationarity of the discrete action for the two adjacent segments leads to the linear system

$$\mathbf{0} = D_2 g(\mathbf{x}_{n-1}, \mathbf{x}_n) + D_1 g(\mathbf{x}_n, \mathbf{x}_{n+1}) + [D_{22} g(\mathbf{x}_{n-1}, \mathbf{x}_n) + D_{11} g(\mathbf{x}_n, \mathbf{x}_{n+1})] (\widehat{\mathbf{x}}_n - \mathbf{x}_n), \quad (9)$$

where  $D_i$  denotes partial differentiation with respect to the  $i$ -th argument and  $D_{ij} = D_i \circ D_j$ . All required gradient and Hessian blocks are approximated numerically. For example, with a small step  $\epsilon$ ,

$$D_1 g(\mathbf{x}_{n-1}, \mathbf{x}_n) \approx \frac{1}{\epsilon} \begin{bmatrix} g(\mathbf{x}_{n-1} - (\epsilon, 0), \mathbf{x}_n) - g(\mathbf{x}_{n-1}, \mathbf{x}_n) \\ g(\mathbf{x}_{n-1} - (0, \epsilon), \mathbf{x}_n) - g(\mathbf{x}_{n-1}, \mathbf{x}_n) \end{bmatrix}, \quad (10)$$

and analogous stencils are used for  $D_2$  and the mixed second derivatives.

To moderate possible overshoot we scale every Newton step by a relaxation coefficient  $0 < \rho < 1$ :

$$\mathbf{x}_n \leftarrow \mathbf{x}_n + \rho (\widehat{\mathbf{x}}_n - \mathbf{x}_n). \quad (12)$$

Once all interior indices  $n = 2, \dots, L-1$  have been displaced, the algorithm possesses an updated polyline  $\Gamma^{\text{new}}$ .

Because the Bézier stage already guarantees obstacle clearance, any tentative point  $\widehat{\mathbf{x}}_n$  that would place the segment  $(\mathbf{x}_{n-1}, \widehat{\mathbf{x}}_n)$  on land is discarded, i.e. we keep the former value of  $\mathbf{x}_n$ . In this way, feasibility is preserved throughout the refinement. After every sweep, segment times are recalculated by forward accumulation, thereby keeping the spatio-temporal schedule consistent with the new geometry.

Iterations proceed until the global cost fails to decrease by more than a prescribed tolerance over two consecutive sweeps. The relaxation parameter  $\rho$  in (12) therefore plays the role of a step-size controller, trading convergence speed against numerical stability.

The hybrid workflow, CMA-ES for coarse search followed by FMS for micro-local polishing, therefore delivers trajectories that are at once globally competitive and rigorously optimal in the small. The evolutionary stage casts a wide net, finding admissible curves that respect land constraints C2; the variational stage then contracts to a stationary point of the discrete action, ensuring that no first-order descent direction remains C7. Because both stages evaluate costs and constraints on densely sampled route discretizations, mid-segment effects are explicitly accounted for, thereby upholding criterion C1.

Our FMS implementation is written in Python and relies on JAX for vectorized arithmetic together with just-in-time compilation [22]. Two run-time knobs are exposed to users:

- **Relaxation coefficient  $\rho$ .** The factor in (12) that scales each Newton increment. Larger values accelerate convergence but can provoke oscillations. We use  $\rho = 0.5$ .
- **Stopping tolerance.** The iteration halts when the relative decrement of the global cost falls below  $10^{-12}$ .

### 3. Benchmark

We evaluated BERS on five well-established vector fields from the literature, each exhibiting distinct characteristics that will be detailed in this section. Table 2 provides a summary of these vector fields, the corresponding optimization objectives, and the results obtained.

Although synthetic, these benchmarks are conservatively constructed to be challenging. Vector fields such as Four Vortices include strong counterflows that limit manoeuvrability, particularly when the surrounding currents approach the magnitude of the vessel’s speed. In parallel, the Perlin-generated landmasses introduce complex topological structures, often more intricate than those encountered along real-world coastlines.

#### 3.1. Circular Vector Field

Originally formulated by Tegy *et al.* [28], the Circular vector field models a rigid-body rotational flow centred at the origin. The field induces uniform circular trajectories across the plane, governed by the angular velocity  $\omega$ :

$$\mathbf{w}(x, y) = \begin{bmatrix} -\omega y \\ \omega x \end{bmatrix}, \quad (13)$$

where  $\omega \in \mathbb{R}$  controls the rotational direction and speed. Positive values correspond to counter-clockwise flow, while negative values induce clockwise motion. In this benchmark, we set  $\omega = -0.9$ , resulting in clockwise rotation.

The routing task consists of identifying the optimal-time route from  $\mathbf{x}_A = (\cos(\pi/6), \sin(\pi/6))$  to  $\mathbf{x}_B = (0, 1)$ , under the constraint of constant unit vessel speed. As the vector field imparts a uniform angular velocity, it offers a clean test bed for assessing trajectory planning and control strategies in rotational flow environments.

The assumption of fixed vessel speed satisfies C5, ensuring that any time optimization is performed within the bounds of realistic propulsion constraints. These simple, controlled conditions make the Circular field a natural starting point for validating weather routing algorithms. While it lacks environmental complexity, it serves to confirm baseline behaviour under constant-speed assumptions. The following vector fields will continue to test this criterion while introducing additional challenges, such as spatial nonlinearity and temporal dynamics.

#### 3.2. Four-Vortices Vector Field

This vector field, originally introduced by Ferraro *et al.* [14], is constructed by superimposing four rotational flow components centred at fixed locations. It is defined by:

$$\mathbf{w}(x, y) = s(-R_{2,2}(x, y) - R_{4,4}(x, y) - R_{2,5}(x, y) + R_{5,1}(x, y)), \quad (14)$$

where each vortex component  $R_{a,b}(x, y)$  takes the form:

$$R_{a,b}(x, y) = \frac{1}{3((x-a)^2 + (y-b)^2) + 1} \begin{bmatrix} -(y-b) \\ x-a \end{bmatrix}, \quad (15)$$

where the scalar  $s = 1.7$  is selected to limit the maximum flow speed to approximately 1. The optimization goal is to compute a time-optimal trajectory from  $\mathbf{x}_A = (0, 0)$  to  $\mathbf{x}_B = (6, 2)$ , under a fixed-speed constraint of 1 unit. Ferraro *et al.* [14] reported an optimal travel time of  $T = 8.95$  under these conditions.

Each vortex decays with the square of distance from its centre, generating sharp local velocity gradients. These induce non-linearities in the cost landscape, requiring

Table 2: Synthetic current environments employed to benchmark the performance of the BERS framework across various routing scenarios and objectives. The table contrasts the best-known results from prior studies with those achieved by BERS, as detailed in Section 4.

Vector Field	Formula	Time dependent?	Origin	Goal	Cost Func.	Ref. Cost	BERS Cost	Comp. Time (s)
Circular [28]	Eq. (13)	No	$(\cos(\frac{\pi}{6}), \sin(\frac{\pi}{6}))$	(0, 1)	Time	1.98	1.98	3
Four Vortices [14]	Eq. (14)	No	(0, 0)	(6, 2)	Time	8.95	8.95	23
Double Gyre [29]	Eq. (17)	Yes	(1.5, 0.5)	(0.5, 0.5)	Time	1.01	1.01	25
Techy [28]	Eq. (18)	Yes	$(\cos(\frac{\pi}{6}), \sin(\frac{\pi}{6}))$	(0, 1)	Time	1.03	1.03	16
Swirllys [14]	Eq. (19)	No	(0, 0)	(6, 5)	Fuel	5.73	1.97	214

continuous trajectory optimization and sufficiently dense along-path evaluation to capture optimal paths. Otherwise, narrow low-cost channels between vortex cores may be missed between sampled points, motivating criterion C1.

### 3.3. Double-Gyre Vector Field

The Double-Gyre vector field, originally introduced by Shadden *et al.* [29], models a time-periodic, two-dimensional flow pattern that approximates features of large-scale geophysical circulations. It has been further explored in oceanographic studies [30]. The system is parametrised by  $A$  (amplitude),  $\epsilon$  (oscillation strength), and  $\omega$  (temporal frequency), with  $t$  denoting time.

We define the following auxiliary functions:

$$\begin{aligned}
 a(t) &= \epsilon \sin(\omega t), \\
 b(t) &= 1 - 2\epsilon \sin(\omega t), \\
 f(x, t) &= a(t)x^2 + b(t)x, \\
 \frac{\partial f}{\partial x}(x, t) &= 2a(t)x + b(t).
 \end{aligned} \tag{16}$$

The time-dependent velocity field is then given by:

$$\mathbf{w}(x, y, t) = \begin{bmatrix} -\pi A \sin(\pi f(x, t)) \cos(\pi y) \\ \pi A \cos(\pi f(x, t)) \sin(\pi y) \frac{\partial f}{\partial x}(x, t) \end{bmatrix}, \tag{17}$$

where  $\epsilon > 0$ ,  $\omega > 0$ , and  $t \in \mathbb{R}$ . The system reduces to a steady-state Hamiltonian flow in the limit  $\epsilon \rightarrow 0$ .

In this benchmark, the goal is to compute the minimum-time trajectory from  $\mathbf{x}_A = (1.5, 0.5)$  to  $\mathbf{x}_B = (0.5, 0.5)$ , assuming a unit vessel speed. Due to the time-varying nature of the flow, this scenario poses challenges for routing algorithms that must account for both spatial structure and temporal evolution.

This case directly addresses C3, as the optimizer must account for changing flow fields over time. Unlike static fields where all forces are known a priori,

time-dependent systems require careful synchronization between spatial routing and temporal evolution. BERS handles this by propagating time forward through the route and adjusting intermediate waypoints accordingly.

### 3.4. Techy Vector Field

This benchmark is derived from a time-dependent vector field originally proposed by Techy *et al.* [28] and later adapted in maritime routing contexts by Mannarini *et al.* [31]. It introduces temporal dynamics into the planning problem via the following expression:

$$\mathbf{w}(x, y, t) = \begin{bmatrix} sx - (t - 0.5)y \\ (t - 0.5)x + sy \end{bmatrix}, \tag{18}$$

where the scalar  $s = -0.3$  controls the strength of a background spiral flow. The routing task consists of finding the minimal-time trajectory from  $\mathbf{x}_A = (\cos(\pi/6), \sin(\pi/6))$  to  $\mathbf{x}_B = (0, 1)$ , assuming a constant ship velocity of 1.

The temporal component of the vector field  $\mathbf{w}(\mathbf{x}, t)$  induces a dynamic reorientation of flow, causing directional variations in the current as time progresses. The system transitions from clockwise to counter-clockwise rotation around the origin depending on whether  $t < 0.5$  or  $t > 0.5$ . As a result, optimal routing must carefully synchronize vessel movement with these transient flow regimes to exploit favourable currents and avoid resistance.

This scenario serves as another focused test of C3, requiring the optimizer to respond to temporally evolving forces. Unlike purely spatial flows, the best path here depends not only on position but also on when each segment is traversed.

### 3.5. Swirllys Vector Field

Originally described by Ferraro *et al.* [14], the Swirllys field couples two non-linear shear components to generate a spatially varying swirl. Its mathematical definition is as follows:

$$\mathbf{w}(x, y) = \begin{bmatrix} \cos(2x - y - 6) \\ \frac{2}{3} \sin(y) + x - 3 \end{bmatrix}. \quad (19)$$

The task is to compute a trajectory from  $\mathbf{x}_A = (0, 0)$  to  $\mathbf{x}_B = (6, 5)$  that minimizes an energy-based cost functional, subject to a fixed travel duration of  $T = 30$ . The cost of moving between points  $\mathbf{x}_{i-1}$  and  $\mathbf{x}_i$  is given by:

$$F(\mathbf{x}_{i-1}, \mathbf{x}_i) = \frac{1}{2} \left\| \frac{\mathbf{x}_i - \mathbf{x}_{i-1}}{t_i - t_{i-1}} - \mathbf{w}(\mathbf{x}_{i-1}, t_{i-1}) \right\|^2 \quad (20)$$

In the equation above,  $\mathbf{w}(\mathbf{x}, t)$  denotes the current field. Although  $\mathbf{w}$  is time-independent in this case, the optimizer must determine both spatial locations and the timing of each segment within the total allowed duration.

This scenario is particularly suited to evaluating C6. Due to the generous total travel time ( $T = 30$ ), the optimizer is not simply minimising distance, but must instead plan a route that meets the arrival deadline while minimising energy expenditure. This encourages solutions that slow down, take detours, or even incorporate loops to remain within the timing constraint. As shown in Ferraro *et al.* [27], such behaviour (though rare in operational contexts) highlights an algorithm’s capacity to handle Just-in-Time (JIT) constraints realistically and efficiently.

In addition, the use of a fuel-based cost function introduces a more complex objective compared to traditional time minimization. This demonstrates the flexibility of our method in handling diverse performance criteria, supporting C4. BERS’s ability to adapt its optimization strategy to different cost structures (while simultaneously satisfying strict timing requirements) makes Swirls a valuable test case in evaluating real-world applications.

### 3.6. Land Generation

To evaluate obstacle handling under diverse topologies, we generate synthetic coastlines with controlled complexity using Perlin noise. In the main text we only retain the benchmark complexity levels (Table 5), which are sufficient to interpret the routing results. The full procedural generation pipeline, interpolation details, and reproducibility settings are provided in Appendix B.

## 4. Validation on Synthetic Vector Fields

All experiments were run using Python 3.12 and JAX 0.4.33 on an NVIDIA RTX A6000 GPU with CUDA 12.6. For reproducibility, all library versions are publicly documented in our shared repository.

### 4.1. Results on Literature Vector Fields

We start by testing BERS on a set of synthetic vector fields previously explored in the literature (Table 2). These cases provide a baseline to check whether BERS, in the absence of obstacles, can match or improve upon existing methods. This also helps evaluate the performance of CMA-ES and FMS independently.

For this analysis, we focus on the effect of two parameters: the number of Bézier control points  $K$ , which controls how complex the resulting curve can be, and the initial standard deviation  $\sigma_0$  of CMA-ES. The rest of the parameters are fixed, since their influence on the optimization is mostly straightforward. We fix the number of waypoints at  $L = 200$  to ensure curves remain smooth and continuous. The CMA-ES population size is set to  $P = 500$ , which we found large enough to work well without significantly increasing computational cost. Algorithm tolerances are set low enough to match the precision of the results reported in the literature. Table 3 lists the full parameter setup.

<b>Bézier configuration</b>	
N. control points, $K$	{3, 6, 9, 12, 15, 18}
N. pieces, $C$	1
N. waypoints, $L$	200
<b>CMA-ES configuration</b>	
Population size, $P$	500
Init. std, $\sigma_0$	{0.5, 1.0, 1.5, 2.0, 2.5, 3.0}
Tolerance	1e-3
<b>FMS configuration</b>	
Damping	0.5
Tolerance	1e-6

Table 3: Parameter configurations used in the experimental evaluation of BERS, for every one of the five vector fields described in Section 3.

We run the full BERS five times on each vector field, each time using a different random seed for CMA-ES. Figure 2 shows how many iterations each configuration needed to converge (on average), and how much cost reduction it achieved compared to the literature. A reduction of zero (white in the color maps) is already a good outcome: it means CMA-ES matches the best known result. Blue regions indicate better performance, where the method found improved solutions. Red regions are configurations that struggled, while black cells indicate cases where the optimizer couldn’t even converge to a feasible solution, typically due to strong currents blocking progress.

Looking at Figure 2, a few patterns stand out. First,  $\sigma_0$  doesn’t seem to affect the number of iterations much,

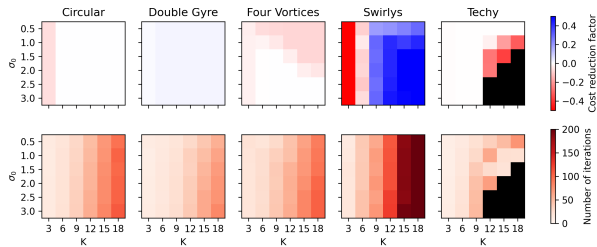


Figure 2: Cost reduction achieved by CMA-ES compared to the literature, and iteration count to convergence, as a function of initial standard deviation  $\sigma_0$  and control points  $K$ . Black cells indicate non-convergent runs.

which is surprising considering that it directly changes the search radius. This suggests that the population is large enough to cover the space regardless of starting spread. On the other hand,  $K$  has a clear impact: more control points mean more parameters to optimize (two per point), which increases the search space. It also affects the quality of the solution, although that depends heavily on the specific vector field. Circular, Double Gyre, and Swirls benefit from higher  $K$  values, while Four Vortices and Techy actually perform worse. For Techy in particular, increasing  $K$  makes convergence harder. We found that setting  $\sigma_0 = 2.0$  and  $K = 9$  gave the best overall performance across the board.

Figure 3 illustrates that FMS yields the greatest benefit when CMA-ES outputs are of lower quality, indicating that it acts as a convergence equalizer across poor initial guesses.

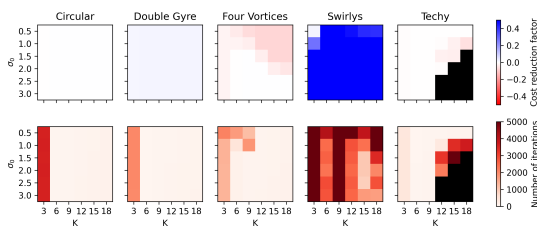


Figure 3: FMS gain ( $\Delta$  cost improvement) as a function of initial CMA-ES quality. Larger gains occur when CMA-ES alone performs poorly.

#### 4.2. Ablation Study: Component Effectiveness

We compare the performance of CMA-ES alone (using  $\sigma_0 = 2.0$  and  $K = 9$ ), FMS alone, and their combined use in BERS. This serves as an ablation to highlight the necessity of the two-stage architecture. In the original work that introduced FMS [14], multiple random initial guesses were used. Here, we opt for the straight-line path as a simple and reproducible baseline, and 200 waypoints to match the CMA-ES resolution.

Vector Field	Ref. Cost	CMA-ES Cost	FMS Cost	BERS Cost
Circular [28]	1.98	1.98	1.98	1.98
Four Vortices [14]	8.95	8.95	9.69	8.95
Double Gyre [29]	1.01	0.99	0.99	0.99
Techy [28]	1.03	1.03	1.04	1.03
Swirls [14]	5.73	3.39	5.59	1.97

Table 4: Results on synthetic vector fields comparing CMA-ES, FMS, and the full BERS pipeline.

In general, CMA-ES and FMS both perform close to the reference values, particularly on simpler vector fields. Notably, CMA-ES alone takes approximately 1 second to converge across all test cases, typically requiring 50 generations (2,500 function evaluations parallelized per generation, for a total of 25,000 evaluations). In contrast, FMS initialized from a straight line can take up to 40 seconds and roughly 50,000 function evaluations. These evaluations are sequential and therefore more computationally demanding.

When combining both stages in BERS, the output of CMA-ES already provides a good-quality path, which significantly reduces the refinement effort. In practice, FMS converges in fewer than 100 iterations in this case, making the total runtime of the full pipeline under 5 seconds. The most noticeable improvements are found in the more complex vector fields, particularly Swirls, where BERS clearly outperforms both algorithms performing on their own.

The ability of BERS to match or exceed performance on Circular and other steady-state vector fields validates its handling of fixed propulsion constraints, satisfying C5.

Figure 4 shows the difference in behaviour between CMA-ES and FMS on the Four Vortices field. CMA-ES explores the search space more broadly, while FMS, starting from a straight line, tends to converge to a nearby local solution. When combined, the full BERS pipeline takes advantage of both strategies and recovers the best result reported in the literature. This is consistent with C1, since route costs are evaluated on dense discretizations that resolve strong mid-segment gradients.

The Double Gyre and Techy vector fields introduce time dependence, with evolving flow structures over the course of the route. BERS successfully achieves the optimal results reported in the literature, demonstrating its ability to adapt to temporally varying environments. This satisfies C3, which requires the optimizer to respond to changing weather or ocean current patterns over time.

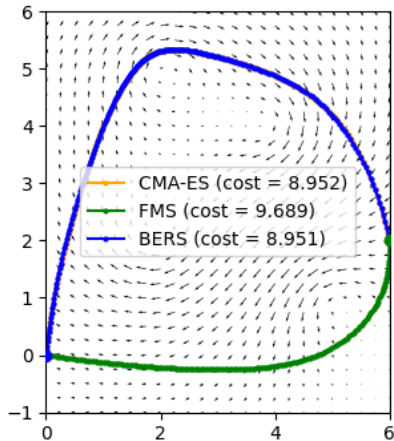


Figure 4: Routes obtained by the CMA-ES algorithm alone (orange), by the FMS algorithm initialized with a straight line (green), and by BERS (blue) on the Four Vertices synthetic field (14).

It is worth mentioning that in the case of Techy, BERS actually achieves a slightly lower cost, but the difference is so small (and the resulting paths so visually similar) that we attribute it to numerical differences rather than any meaningful performance gain.

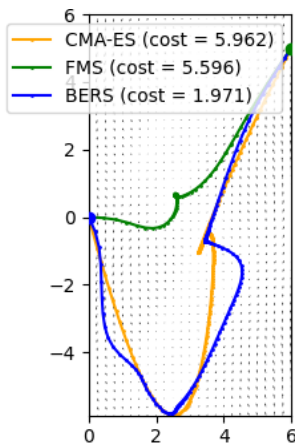


Figure 5: Route obtained by BERS in the Swirls vector field under a fuel minimization objective with fixed arrival time  $T = 30$ . The initial solution from CMA-ES is shown in orange, and its refined counterpart via FMS appears in blue. For comparison, the green curve shows the FMS result when initialized from a direct line segment.

The Swirls vector field is particularly challenging due to its fixed travel-time constraint ( $T = 30$ ). This scenario is a strong test of C6, as the optimizer must adhere to the schedule while minimising energy use. Figure 5 shows how BERS successfully navigates this trade-off by adjusting trajectory shape and timing. In this case, BERS identifies a more energy-efficient path than

that reported by Ferraro *et al.* [27]. It is worth noting, however, that the authors’ objective in that work was not to optimize for the vector field itself, but rather to demonstrate the general convergence behaviour of their algorithm.

Additionally, the Swirls case uses a fuel consumption model instead of a traditional time-minimization objective. BERS’s ability to handle this alternate cost structure, while still delivering high-quality routes, demonstrates support for C4. Thanks to the generality of CMA-ES and the compatibility of FMS with non-differentiable or custom cost models, BERS can adapt to a wide range of optimization goals.

Together, these experiments demonstrate that BERS satisfies multiple criteria of a comprehensive weather routing algorithm, including spatial continuity, obstacle handling, dynamic adaptation, timing constraints, and cost-function flexibility.

#### 4.3. Results on Land Avoidance

After validating BERS in open-water scenarios, we now test whether it can handle geographic constraints, specifically routing through environments in which land-masses block direct paths. This experiment directly targets C2, which requires feasible routing in the presence of static hazards. It also probes C1, because land interactions are computed through dense intra-segment sampling rather than only at waypoint locations.

To avoid oversimplification, we retain the Four Vortices vector field and superimpose land obstacles, thereby combining strong flow dynamics with spatial constraints. We define three levels of land complexity based on the land-generation parameters introduced in Section 3.6:

Table 5: Land complexity levels used in benchmarking.

Complexity Level	Resolution	Water Level
Easy	3	0.9
Medium	4	0.8
Hard	5	0.7

For each level, we generate 50 random land configurations and run the full BERS pipeline to compute a path from  $(0, 0)$  to  $(6, 2)$ . The goal is to recover a high-quality route that respects land constraints and still benefits from the vector field.

Figure 6 shows the average travel time and computation time across the three complexity settings. As expected, more land (i.e., lower water level and higher resolution) leads to longer travel times and higher computational costs. Notably, most of the time is spent during

the CMA-ES stage, which faces an increasingly difficult search problem. FMS remains fast, but its contribution grows more important as land constraints become tighter.

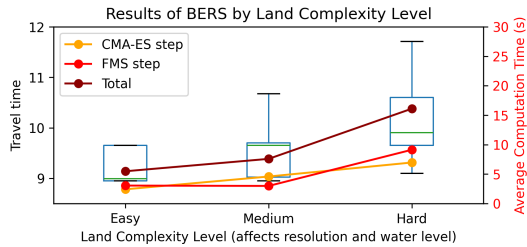


Figure 6: Performance of BERS across increasing land complexity. Left axis shows a box-plot of travel times over 50 random instances; right axis shows average computation time, decomposed into CMA-ES and FMS steps.

To better understand how the two stages behave in practice, Figures 7 to 9 show three example runs, one from each complexity level. The blue curve is the final output of BERS, while the orange curve shows the raw CMA-ES result before refinement. The background flow (Four Vortices) and land patches (black) are also shown.

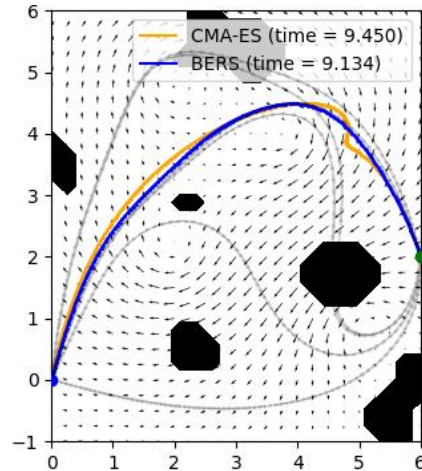


Figure 8: Representative result in a **medium** scenario. FMS slightly improves the CMA-ES path.

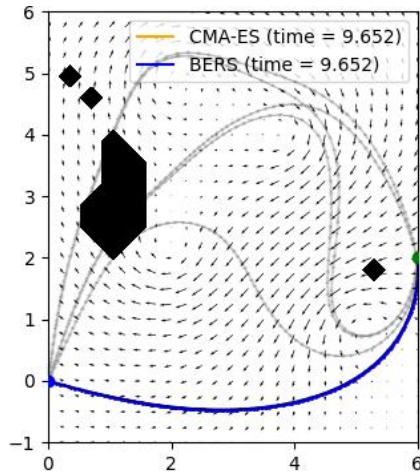


Figure 7: Representative result in an **easy** scenario. CMA-ES alone already converges to the locally optimal path.

In the easy setting (Figure 7), CMA-ES already finds a clean solution and FMS makes only minor adjustments. The gray curves indicate the locally optimal paths reported by Ferraro *et al.* [27]. In this instance, BERS follows the only previously identified viable path that remains unobstructed. In the medium case (Figure 8), BERS again recovers one of the paths reported by Ferraro *et al.* [27]. The hard case (Figure 9) is more demanding: all previously known paths are blocked by land, and BERS must identify a new one. CMA-ES initially

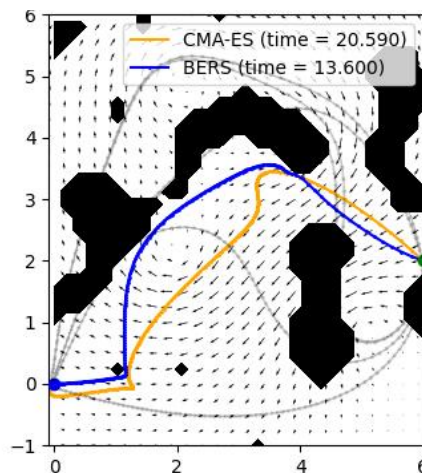


Figure 9: Representative result in a **hard** scenario. CMA-ES finds a feasible but inefficient path, which FMS significantly improves.

converges to a long detour, which FMS then corrects, recovering a trajectory much closer to the land-free optimum. The refinement step also smooths route transitions near the land boundary.

This pattern highlights the complementary strengths of both stages. CMA-ES handles global feasibility, especially useful when corridors are narrow or fragmented, while FMS improves curvature and removes detours introduced by optimization noise or local minima. Together, they produce results that remain close to those reported in the literature, even under tight constraints. These examples confirm that BERS satisfies C1 by accounting for mid-segment effects through dense sampling, alongside C2 and C3, while reinforcing the importance of local optimization in complex environments (C7).

## 5. Results on Real Ocean Data

Building on the synthetic validation in Section 4, we assess BERS on two trans-oceanic routing scenarios involving a cargo vessel equipped with a Wind Propulsion System (WPS). In this context, route optimization and wind conditions interact in both propulsion modes: the optimizer reduces aerodynamic drag and exploits favourable wave conditions regardless of WPS mode, and additionally seeks apparent wind angles that maximize wingsail thrust when WPS is enabled. We use the Just-in-Time cost formulation of Criterion C6, replacing the quadratic surrogate of Section 2.3 with a physics-based ship performance model, and evaluate all configurations over a full year of ERA5 reanalysis data. Throughout the following results, all reported energy costs reflect *real* propulsive energy only. Internally, the algorithms optimize against a *penalized* cost function that adds soft penalties for constraint violations (Section 2.4: wind-speed and wave-height thresholds). When interpreting results, especially FMS refinement, note that FMS may accept a small increase in real propulsive energy in exchange for a substantial reduction in weather-related constraint violations, thereby lowering the penalized optimization objective and improving practical route feasibility. The energy values shown here exclude these artificial penalty terms.

### 5.1. Experimental Setup

We consider a generic 88 m single-skeg cargo vessel equipped with four 138 m<sup>2</sup> rigid wingsails (552 m<sup>2</sup> total sail area), a controllable-pitch propeller, and electric propulsion. Net propulsive power is computed at each waypoint with a physics-based performance model that

includes hull resistance, aerodynamic drag, wave-added resistance, and, when WPS is enabled, wingsail thrust as a function of apparent wind angle, true wind speed, significant wave height, and vessel speed. The optimization objective is total voyage energy (MWh). We evaluate this model on two trans-oceanic corridors (Table 6): a Trans-Atlantic leg from Santander (Spain) to New York (USA), and a Trans-Pacific leg from Tokyo (Japan) to Los Angeles (USA). The assigned passage times are fixed at 354 h and 583 h, respectively, thereby enforcing Criterion C6. Under this fixed-time formulation, instantaneous vessel speed at each waypoint is determined by local route geometry and total voyage duration.

Table 6: Trans-oceanic corridors used in the real-ocean experiments.

Corridor	Origin	Destination	GC Dist. (nm)	Pass. Time (h)
Atlantic	Santander (ESSDR)	New York (USNYS)	2826	354
Pacific	Tokyo (JPTYO)	Los Angeles (USLAX)	4663	583

Environmental forcing is provided by official ERA5 reanalysis fields for 2024, including 10 m wind, significant wave height (SWH), and mean wave direction [32]. The underlying data are available on a 0.25° grid at 1-hour intervals, and route-wise environmental values are evaluated by tricubic interpolation in space and time. Safety limits are enforced through the soft-penalty formulation introduced in Section 2.4, using wind-speed and wave-height thresholds of 20 m/s and 7 m, respectively. For each corridor, we study two routing strategies (great-circle baseline and BERS-optimized) and two propulsion modes (WPS enabled/disabled), yielding eight experimental configurations. Each configuration is evaluated for all 366 daily departures at 12:00 UTC in 2024.

For optimized routes, we report both CMA-ES-only solutions and the full two-stage BERS pipeline (CMA-ES followed by FMS). CMA-ES is configured with  $K = 10$  control points,  $L = 100$  waypoints, and initial standard deviation  $\sigma_0 = 0.1$ , initialized from the great-circle trajectory. FMS refinement then uses the same relaxation and stopping criteria described in Section 2.5.

### 5.2. Route Geometry

Figure 10 shows representative optimized routes for both corridors, coloured by departure season. For visual clarity, the figure displays one optimized route per month for each corridor, selected from the full set of daily departures. The mean route length for the full BERS pipeline is 3,078 nm (Trans-Atlantic) and 4,884 nm (Trans-Pacific), compared with great-circle distances of 2,826 nm and 4,663 nm, respectively. Winter routes (blue) exhibit the largest deviations from the great-circle

baseline, consistent with the stronger synoptic forcing encountered during that season. The broad spread of trajectories across each corridor indicates that BERS explores a wide range of feasible route geometries in response to changing weather conditions. In several cases, the optimized routes approach the coastline closely, effectively following shorelines where winds and waves may be more moderate, yet they do so without violating land constraints. If a larger safety margin from the coast were required, the modular structure of BERS would allow the inclusion of an additional shoreline-proximity penalty, for example through a quadratic cost term that increases as the route approaches land.

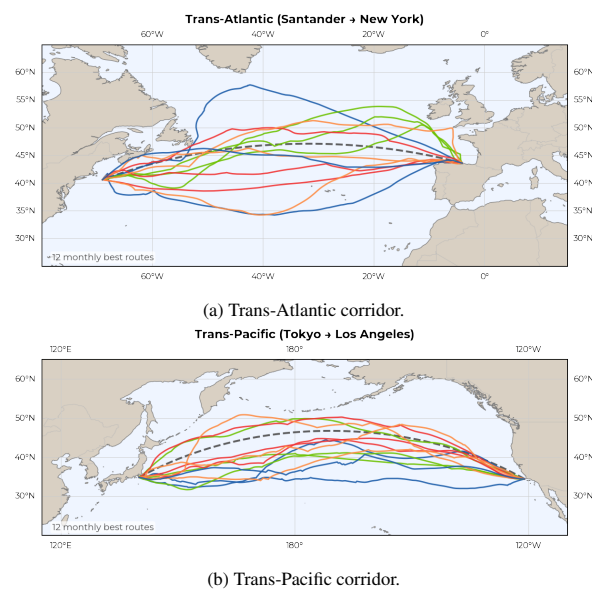


Figure 10: Representative optimized routes (BERS) versus the great-circle baseline (dashed). Departures are colored by season: spring in green, summer in red, autumn in yellow, winter in blue.

### 5.3. Energy Savings from Route Optimization

Figure 11 shows the Trans-Atlantic energy distributions with and without WPS across all 366 departures. For brevity, we display the Atlantic distributions only; the Pacific corridor exhibits the same qualitative behaviour and is summarized numerically in Table 7. Two patterns are consistent across strategies: (1) great-circle (GC) routes exhibit a broader high-energy tail, indicating departures under extreme weather where adaptive routing can avoid costly exposure; and (2) enabling WPS shifts distributions downward in all strategies, with a slightly longer low-energy tail than in the no-WPS case, showing that favourable wind scenarios can produce especially large reductions.

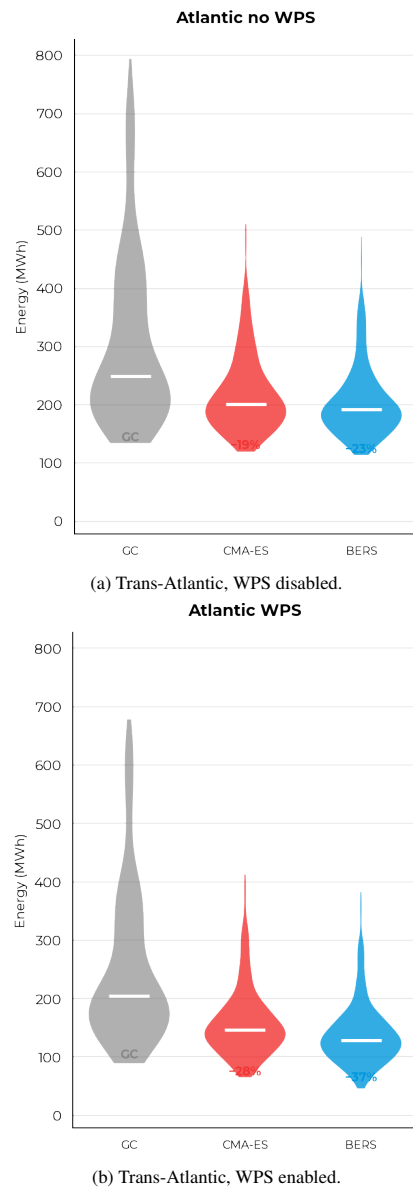


Figure 11: Voyage energy distribution (MWh) across 366 departures of 2024 for each experimental configuration. Great-circle baseline in grey, CMA-ES optimized routes in red, BERS in blue.

Table 7: Mean voyage energy and energy savings for all experimental configurations across 366 departures of 2024. “Saving vs GC<sub>same</sub>” compares optimized to the great-circle baseline of the same WPS mode; “Saving vs GC<sub>noWPS</sub>” compares to the propulsion-only great-circle baseline.

Corridor	WPS	Strategy	Mean (MWh)	Std (MWh)	Saving vs GC <sub>same</sub> (%)	Saving vs GC <sub>noWPS</sub> (%)
Atlantic	Disabled	Great Circle	310.3	148.7	—	—
Atlantic	Disabled	CMA-ES	220.2	67.0	29.0	29.0
Atlantic	Disabled	BERS	206.2	61.3	33.6	33.6
Atlantic	Enabled	Great Circle	253.3	133.9	—	18.4
Atlantic	Enabled	CMA-ES	159.9	59.1	36.9	48.5
Atlantic	Enabled	BERS	139.5	52.7	44.9	55.0
Pacific	Disabled	Great Circle	251.7	84.7	—	—
Pacific	Disabled	CMA-ES	200.2	22.5	20.5	20.5
Pacific	Disabled	BERS	194.8	20.3	22.6	22.6
Pacific	Enabled	Great Circle	158.0	72.1	—	37.2
Pacific	Enabled	CMA-ES	87.3	26.3	44.8	65.3
Pacific	Enabled	BERS	64.1	31.6	59.4	74.5

Route optimization by CMA-ES alone reduces mean voyage energy by 21–45% relative to the great-circle baseline of the same WPS mode. The full BERS pipeline extends these gains to 23–59%. The largest absolute benefit is on the Trans-Pacific corridor with WPS enabled, where BERS cuts mean energy from 158.0 MWh (GC) to 64.1 MWh, a reduction of 59.4%. Without WPS on the same corridor, the optimizer reduces aerodynamic drag alongside hull-resistance and wave-added resistance, but cannot harvest wind thrust, yielding a more modest 22.6% saving.

#### 5.4. Effect of Wind Propulsion System

Comparing the with/without-WPS columns in Table 7 shows the effect of wind assistance for the same routing strategy. On the great-circle route, WPS reduces mean energy by 57 MWh (18.4%) on the Atlantic and 94 MWh (37.2%) on the Pacific. When combined with BERS route optimization, the WPS benefit grows to 67 MWh (32.3%) and 131 MWh (67.1%), respectively, because, beyond the aerodynamic drag reduction and wave avoidance available regardless of WPS mode, the optimized route also actively seeks apparent wind angles that maximize wingsail thrust. Combining BERS routing with WPS reduces mean voyage energy by 55.0% (Atlantic) and 74.5% (Pacific) compared with a propulsion-only great-circle voyage.

#### 5.5. FMS Refinement in the Real-World Setting

Figure 12 shows per-departure energy for CMA-ES alone against the full BERS pipeline. The majority of

points lie below the diagonal, confirming that FMS substantially improves the route for most departures. The additional mean saving from FMS over CMA-ES ranges from 2.7% (Pacific, no WPS) to 26.5% (Pacific, WPS enabled), with 12.8% and 6.4% for the Atlantic WPS and no-WPS cases, respectively. The improvement is largest for low-energy WPS configurations, where the non-convex energy landscape shaped by wingsail thrust contains many local minima. In those cases, FMS descends from the CMA-ES solution to a better nearby optimum. For cases where FMS refinement appears to increase the real energy cost while improving the optimization objective, the explanation lies in constraint violation reduction: FMS actively trades small increases in propulsive energy for substantial reductions in weather-related constraint violations. This trade-off is beneficial because the penalization strategy (Section 2.4) strongly penalizes routes with high winds or waves. By accepting marginally longer routes with safer weather exposure, FMS reduces the overall optimization cost and improves practical feasibility. Indeed, FMS substantially enforces safety-constraint feasibility: wave-height violations fall from 4.6–22.1% of departures (CMA-ES) to 0.8–1.4% (full BERS). For reference, the great-circle baseline has wave-height violations on 19% (Atlantic) and 36% (Pacific) of departures and wind violations on 12% and 26%, reflecting the consequence of not adapting to weather conditions. A complete per-configuration breakdown of both thresholds is omitted here for brevity; the wave-height rates are reported explicitly as a representative safety diagnostic. The large standard deviations for GC

in Table 7 arise partly from these high-penalty departures.

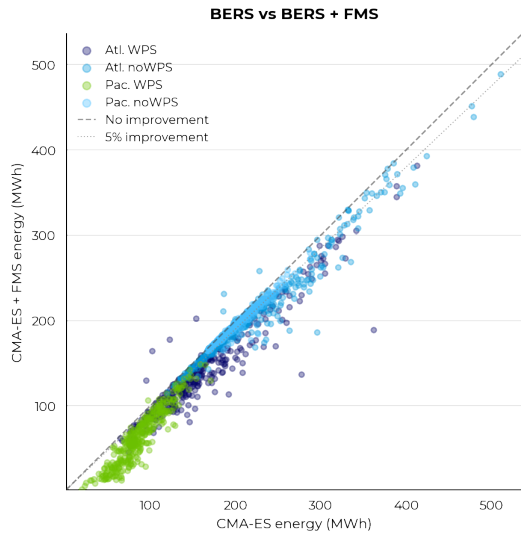


Figure 12: Per-departure voyage energy for CMA-ES alone (x-axis) versus the full BERS pipeline (y-axis). The majority of points lie below the no-improvement diagonal (dashed), showing that FMS refinement consistently reduces energy. The dotted line marks a 5% improvement threshold.

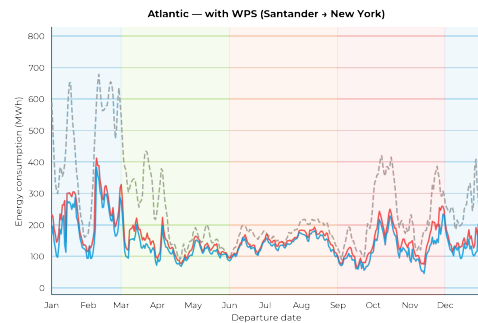
### 5.6. Seasonal Variability

Figure 10 provides representative monthly route geometries that help interpret seasonal patterns. The great-circle baseline exhibits pronounced seasonal oscillations driven by the intensification and weakening of the mid-latitude westerlies, with peaks in winter and troughs in summer. The optimized routes substantially damp this variability: BERS achieves its largest absolute savings in winter, when strong winds simultaneously increase propulsive demand on the great-circle route and provide the greatest sail thrust on optimized routes, and its smallest savings in summer.

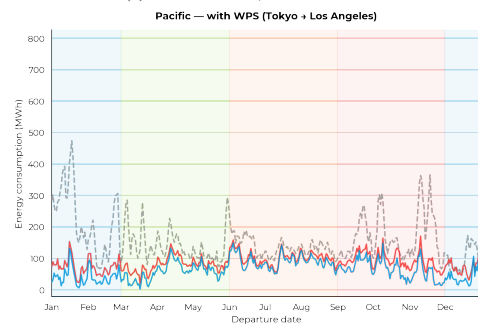
Table 8 summarises seasonal savings of the full BERS pipeline with WPS relative to the WPS great-circle baseline. Winter delivers the highest gains: 53.8% for the Atlantic and 77.0% for the Pacific, reflecting the intense and consistent westerly circulation during boreal winter. Summer savings remain appreciable (20.8% and 33.1%), demonstrating that route optimization provides meaningful benefits throughout the year.

## 6. Discussion

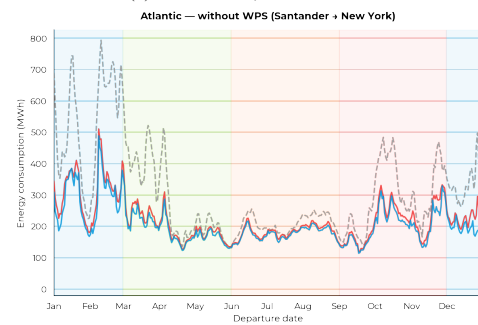
The results of this study show that BERS effectively balances exploration, constraint handling, and solution



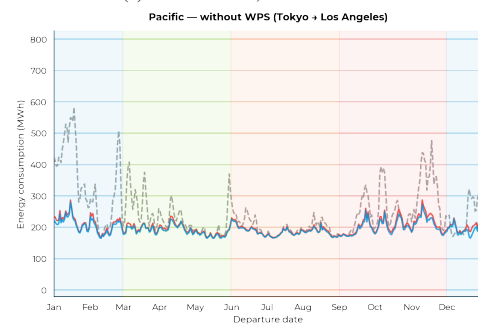
(a) Trans-Atlantic, WPS enabled.



(b) Trans-Pacific, WPS enabled.



(c) Trans-Atlantic, WPS disabled.



(d) Trans-Pacific, WPS disabled.

Figure 13: Daily voyage energy throughout 2024 for the great-circle baseline (dashed grey), CMA-ES alone (red), and full BERS (blue).

Table 8: Seasonal energy savings (%) of the full BERS pipeline with WPS enabled versus the great-circle baseline with WPS.

Season	Atlantic (%)	Pacific (%)
Winter	53.8	77.0
Spring	46.1	58.9
Summer	20.8	33.1
Autumn	47.6	62.2

refinement in the context of maritime weather routing. By combining the global search capabilities of the Covariance Matrix Adaptation Evolution Strategy (CMA-ES) with the local refinement of the Ferraro-Martín de Diego-Sato (FMS) algorithm, BERS meets the proposed criteria for a routing framework within the scope of benchmark tests and real-world data. It produces continuous, obstacle-aware routes, remains adaptable to changing conditions, and supports a range of cost functions.

The results in Section 4 show that, within the benchmark settings, BERS meets the seven criteria introduced earlier. The continuous Bézier representation avoids grid artefacts; the land penalty and FMS refinement preserve feasibility near obstacles; and the two cost formulations cover both time-optimal and fixed-arrival objectives while maintaining constant engine load. The variational stage further enforces the local optimality around the CMA-ES solution. These controlled settings emulate many practical challenges, but do not encompass the full variability of real-world routing.

From a computational perspective, BERS maintains a practical trade-off between quality and runtime. CMA-ES typically converges within seconds. FMS adds cost, especially near land or under complex flow, but is not always required. Selectively applying FMS when CMA-ES fails to produce a well-refined result could significantly reduce the computation time. This strategy could be guided by adaptive stopping criteria or confidence thresholds.

The parameter studies indicate the expected trade-off between expressiveness ( $K$ ) and optimization difficulty, and a context-dependent role for the initial search variance  $\sigma_0$ .

The experiments on real ocean data reveal several consistent empirical trends. The energy savings achieved by BERS vary strongly with WPS configuration and corridor: the Trans-Pacific route with WPS enabled yields the largest gains (up to 59% from routing alone, 75% combined with wingsails), because the extended fetch of the Pacific permits the optimized route to systematically exploit persistent westerlies, while the wingsail thrust

amplifies the benefit of favourable apparent wind angles. The seasonal analysis confirms that winter delivers the highest savings on both corridors, reflecting the intensification of mid-latitude westerlies and the associated increase in available sail thrust during boreal winter. In summer, when westerlies weaken, the gap between optimized and great-circle routes narrows, but energy savings of 21–33% remain appreciable. A second key finding is the synergy between routing and wind assistance: the WPS saving grows from 18–37% on great-circle routes to 32–67% on BERS-optimized routes, because the algorithm actively shapes the trajectory to maximize wingsail utilization rather than treating sail thrust as a passive bonus. Finally, the FMS refinement stage provides consistent improvement over CMA-ES in all cases, especially for WPS-enabled routes where the non-convex energy landscape favours further local descent. It also reduces safety-constraint violations to near zero, confirming that feasibility is a byproduct of FMS convergence. These results demonstrate that the energy savings achievable with wind-assisted vessels under adaptive routing substantially exceed the 0–7% commonly reported for conventional weather routing [8, 11], and highlight the growing relevance of route optimization algorithms for the decarbonization of deep-sea shipping.

These results also reveal a structural limitation of the present study: the experiments cover two specific open-ocean corridors for a single vessel type. Although the corridors are representative of major trans-oceanic trade lanes and the 366-departure design captures a full year of ERA5 variability, the magnitude of savings will depend on vessel dimensions, sail area, propulsion power, and the prevailing wind climatology of the chosen route. Narrow waterways such as the Suez or Panama canals remain challenging for a smooth, low-dimensional trajectory representation: a single continuous Bézier curve with a limited number of control points cannot reliably represent tight, elongated passages without violating feasibility constraints. A hybrid planner that switches to a corridor-constrained method for narrow sections and reconnects to the global Bézier parametrization in open waters would likely address this limitation.

## 7. Concluding Remarks and Future Directions

This paper presented BERS, a two-phase optimization strategy for maritime weather routing that integrates global exploration using CMA-ES with local trajectory refinement through FMS. The method is designed to address key challenges in trajectory planning, including flow adaptation, obstacle avoidance, and scheduling constraints.

Through synthetic benchmarks, BERS demonstrated robust performance in a diverse set of scenarios, including steady-state and time-dependent vector fields, fixed-speed travel, and just-in-time arrival. The algorithm reproduced or improved known optimizations from the literature and maintained feasibility under varying land complexities.

Although these results highlight BERS’s capability to address the proposed criteria within controlled benchmark experiments, synthetic findings alone do not imply universal applicability. For this reason, we also validated the proposed framework on real-world oceanographic data. Experiments on two trans-oceanic corridors (Trans-Atlantic and Trans-Pacific) over 366 departures throughout 2024, using ERA5 reanalysis and a physics-based model for a wind-assisted cargo vessel, showed that BERS produces physically consistent and operationally meaningful routes with substantial energy savings. Route optimization alone achieves 23–59% reduction in mean propulsive energy relative to the great-circle baseline, and combining optimized routing with wingsail technology yields up to 75%, with consistent additional gains from FMS refinement over CMA-ES. These findings reinforce the practical relevance of BERS for maritime decarbonization.

Future work will focus on operational deployment and methodological extensions. An adaptive application of FMS, triggered when CMA-ES results lack smoothness or feasibility, could reduce runtime without degrading quality. For narrow passages, a hybrid planner that switches to a corridor-constrained graph or sampling-based method and then reconnects to the continuous curve would likely be more reliable than a single global parametrization. We also plan to incorporate more realistic cost functions derived from naval engineering models and weather forecasts.

In summary, BERS offers a flexible and modular approach to weather routing, combining the strengths of global evolutionary search with local variational refinement. The real-world experiments demonstrate substantial energy savings for wind-assisted vessels, underlining the algorithm’s potential as a practical tool for maritime decarbonization. Further empirical validation on additional vessel types and corridors, and methodological extensions for narrow-waterway routing, remain as future work.

## Appendix A. Canonical Cost Formulations

For completeness, we include the two canonical benchmark objectives used in prior weather-routing studies.

### Appendix A.1. Travel-Time Objective (Constant Engine Load)

Following the classical Zermelo setting [33], total travel time is minimized under constant vessel speed through water  $S$ :

$$\sum_{n=1}^{L-1} \Delta t_n = \sum_{n=1}^{L-1} \frac{\sqrt{(x_{n+1} - x_n)^2 + (y_{n+1} - y_n)^2}}{w_n \cos(\psi_n) + \sqrt{S^2 - w_n^2 \sin^2(\psi_n)}}. \quad (\text{A.1})$$

Here  $w_n$  is the local field magnitude at  $(x_n, y_n, t_n)$  and

$$\psi_n = \arctan\left(\frac{y_{n+1} - y_n}{x_{n+1} - x_n}\right) - \arctan\left(\frac{v_n}{u_n}\right). \quad (\text{A.2})$$

In time-dependent fields,  $t_n$  must be propagated sequentially along the route, which couples geometry and timing.

### Appendix A.2. Fuel/Energy Objective (Fixed Arrival Time)

For Just-in-Time scenarios, total duration  $T$  is fixed and we map  $t_n = T r_n$  along the normalized curve parameter. Segment cost follows Ferraro *et al.* [14]:

$$\sum_{n=1}^{L-1} F(\mathbf{x}_n, \mathbf{x}_{n+1}) = \sum_{n=1}^{L-1} \frac{1}{2} \left\| \frac{\mathbf{x}_{n+1} - \mathbf{x}_n}{t_{n+1} - t_n} - \mathbf{w}(\mathbf{x}_n, t_n) \right\|^2. \quad (\text{A.3})$$

### Appendix A.3. Feasibility Condition and Modular Objectives

A basic feasibility condition is

$$\frac{w_n}{S} \leq 1, \forall n \in [1, L - 1]. \quad (\text{A.4})$$

Beyond these canonical forms, BERS accepts arbitrary black-box objectives (including proprietary vessel-performance models), because both CMA-ES and FMS depend only on cost evaluations.

## Appendix B. Synthetic Land-Generation Procedure

To stress-test obstacle avoidance, synthetic coastlines are generated with Perlin noise [34, 35]. A normalized scalar field over the spatial domain is thresholded by a water-level parameter to obtain a binary land-water mask. Complexity is controlled by map resolution and threshold, and reproducibility by random seed. During optimization, land interaction is evaluated by interpolating

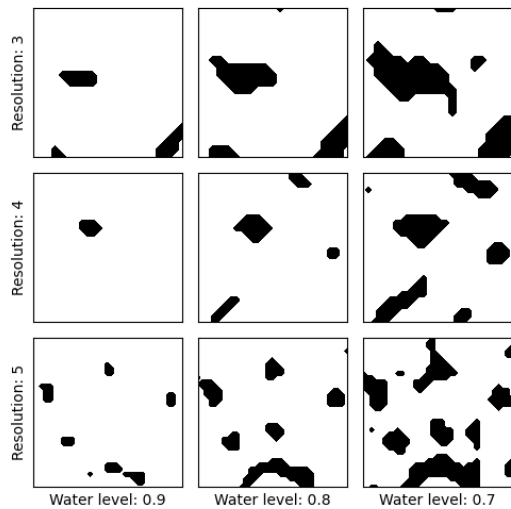


Figure B.14: Different land configurations generated with Perlin noise, fixing the random seed at 4.

each candidate trajectory on a denser sampling and querying the mask with bilinear interpolation (implemented with `jax.scipy.ndimage.map_coordinates`).

Figure B.14 shows representative configurations across increasing resolution and decreasing water level.

### Acknowledgements

This work was carried out within the framework of the BBVA-Funding project “Optimization of maritime routes for a more efficient, safer, and decarbonized maritime transport”. This paper was partially funded by MICIU / AIE / 10.13039/501100011033 / FEDER, UE, Grants No. PID2024-155187OB-I00 (KAN4MET) and PID2021-122154NB-I00 (OP4ML), co-financed by the European Regional Development Fund, “ERDF - A Way of Making Europe”. LB appreciates the support of MITACS (Accelerate award IT26380), which helped finance his research stay in Madrid during the completion of this study.

### References

- [1] D. Precioso Garcelán, Applications of machine learning and data science to the blue economy sustainable fishing and weather routing, Ph.D. thesis, Universidad de Cádiz (2023).
- [2] R. Szlapczynski, J. Szlapczynska, R. Vettor, Ship weather routing featuring w-MOEA/D and uncertainty handling, *Applied Soft Computing* 138 (2023) 110142.

- [3] S. Grandcolas, A metaheuristic algorithm for ship weather routing, *Operations Research* 3 (2022) 35.
- [4] J. J. de-la Jara, D. Precioso, L. Bu, V. Redondo-Neble, R. Milson, R. Ballester-Ripoll, D. Gómez-Ullate, HADAD: Hexagonal A-star with differential algorithm designed for weather routing, *Ocean Engineering* (2024).
- [5] G. Mannarini, M. L. Salinas, L. Carelli, N. Petacco, J. Orović, VISIR-2: ship weather routing in Python, *Geoscientific Model Development* 17 (10) (2024) 4355–4382.
- [6] D. Precioso, R. Milson, L. Bu, Y. Menchions, D. Gómez-Ullate, Hybrid search method for Zermelo’s navigation problem, *Computational and Applied Mathematics* (2024).
- [7] W. Zhao, H. Wang, J. Geng, W. Hu, Z. Zhang, G. Zhang, Multi-objective weather routing algorithm for ships based on hybrid particle swarm optimization, *Journal of Ocean University of China* 21 (1) (2022) 28–38.
- [8] International Maritime Organization, Greenvoyage2050: Ship energy efficiency measures – weather routing, <https://greenvoyage2050.imo.org/>, accessed: 2025-10-09 (2022).
- [9] H. Hagiwara, T. Waseda, Optimization of ship routing considering wave-induced added resistance, *Journal of Marine Science and Engineering* 9 (3) (2021) 259. doi:10.3390/jmse9030259.
- [10] X. Qian, Y. Zhang, P. Li, B. Zhou, Energy-efficient weather routing using reinforcement learning, *Ocean Engineering* 281 (2023) 114969. doi:10.1016/j.oceaneng.2023.114969.
- [11] Sofar Ocean, Fuel and emissions savings from real-time voyage optimization, Tech. rep., Sofar Ocean Technologies, technical Report (2024).
- [12] International Maritime Organization, Fourth imo ghg study 2020, <https://www.imo.org/en/OurWork/Environment/Pages/Fourth-IMO-GHG-Study-2020.aspx>, greenhouse gas emission factors and analysis for international shipping (2020).
- [13] International Maritime Organization, 2023 imo strategy on reduction of ghg emissions from ships, IMO website, adopted by MEPC 80 (Resolution MEPC.377(80)) (2023).

- [14] S. J. Ferraro, D. M. de Diego, R. T. S. M. de Almagro, Parallel iterative methods for variational integration applied to navigation problems, *IFAC-PapersOnLine* 54 (2021) 321–326. doi:10.1016/J.IFACOL.2021.11.097.
- [15] N. Charalambopoulos, E. Xidias, A. Nearchou, Efficient ship weather routing using probabilistic roadmaps, *Ocean Engineering* 273 (2023) 114031. doi:https://doi.org/10.1016/j.oceaneng.2023.114031.
- [16] M. Grifoll, C. Borén, M. Castells-Sanabra, A comprehensive ship weather routing system using CMEMS products and A\* algorithm, *Ocean Engineering* 255 (2022) 111427.
- [17] N. Hansen, S. D. Müller, P. Koumoutsakos, Reducing the time complexity of the derandomized evolution strategy with covariance matrix adaptation (CMA-ES), *Evolutionary Computation* 11 (1) (2003) 1–18.
- [18] P. Bézier, *Numerical control-mathematics and applications*, Translated by AR Forrest (1972).
- [19] G. Farin, *Curves and surfaces for CAGD: a practical guide*, Elsevier, 2001.
- [20] P. De Castel'jau, *Mathématiques et cao. volume 2: formes à pôles* (1985).
- [21] W. Boehm, A. Müller, On de Castel'jau's algorithm, *Computer Aided Geometric Design* 16 (7) (1999) 587–605. doi:https://doi.org/10.1016/S0167-8396(99)00023-0.
- [22] J. Bradbury, R. Frostig, P. Hawkins, M. J. Johnson, C. Leary, D. Maclaurin, G. Necula, A. Paszke, J. VanderPlas, S. Wanderman-Milne, Q. Zhang, *JAX: composable transformations of Python+NumPy programs* (2018). URL <http://github.com/google/jax>
- [23] N. Hansen, *The cma evolution strategy: A tutorial*, arXiv preprint arXiv:1604.00772 (2016).
- [24] N. Hansen, A. Ostermeier, Completely derandomized self-adaptation in evolution strategies, *Evolutionary computation* 9 (2) (2001) 159–195.
- [25] N. Hansen, S. D. Müller, P. Koumoutsakos, Reducing the time complexity of the derandomized evolution strategy with covariance matrix adaptation (cma-es), *Evolutionary computation* 11 (1) (2003) 1–18.
- [26] N. Hansen, Y. Akimoto, P. Baudis, *CMA-ES/pycma* on Github, Zenodo, DOI:10.5281/zenodo.2559634 (Feb. 2019). doi:10.5281/zenodo.2559634. URL <https://doi.org/10.5281/zenodo.2559634>
- [27] S. J. Ferraro, D. Martín de Diego, R. T. Sato Martín de Almagro, A parallel iterative method for variational integration, arXiv preprint arXiv:2206.08968 (2022).
- [28] L. Techy, Optimal navigation in planar time-varying flow: Zermelo's problem revisited, *Intelligent Service Robotics* 4 (4) (2011) 271–283. doi:10.1007/s11370-011-0092-9. URL <https://doi.org/10.1007/s11370-011-0092-9>
- [29] S. C. Shadden, F. Lekien, J. E. Marsden, Definition and properties of lagrangian coherent structures from finite-time lyapunov exponents in two-dimensional aperiodic flows, *Physica D: Nonlinear Phenomena* 212 (3) (2005) 271–304. doi:https://doi.org/10.1016/j.physd.2005.10.007. URL <https://www.sciencedirect.com/science/article/pii/S0167278905004446>
- [30] P. Gunnarson, I. Mandralis, G. Novati, P. Koumoutsakos, J. O. Dabiri, Learning efficient navigation in vortical flow fields, *Nature communications* 12 (1) (2021) 7143.
- [31] G. Mannarini, L. Carelli, VISIR-1. b: Ocean surface gravity waves and currents for energy-efficient navigation, *Geoscientific Model Development* 12 (8) (2019) 3449–3480.
- [32] H. Hersbach, B. Bell, P. Berrisford, S. Hirahara, A. Horányi, J. Muñoz-Sabater, J. Nicolas, C. Peubey, R. Radu, D. Schepers, et al., ERA5 global reanalysis, *Quarterly Journal of the Royal Meteorological Society* 146 (730) (2020) 1999–2049. doi:10.1002/qj.3803.
- [33] E. Zermelo, Über das navigationsproblem bei ruhender oder veränderlicher windverteilung, *ZAMM - Journal of Applied Mathematics and Mechanics* 11 (2) (1931) 114–124. arXiv:https://onlinelibrary.wiley.com/doi/pdf/10.1002/zamm.19310110205, doi:https://doi.org/10.1002/zamm.19310110205.
- [34] K. Perlin, An image synthesizer, *ACM Siggraph Computer Graphics* 19 (3) (1985) 287–296.

- [35] A. Lagae, S. Lefebvre, R. Cook, T. DeRose, G. Drettakis, D. S. Ebert, J. P. Lewis, K. Perlin, M. Zwicker, A survey of procedural noise functions, in: *Computer Graphics Forum*, Vol. 29, Wiley Online Library, 2010, pp. 2579–2600.